Computers and Fluids xxx (2017) xxx-xxx

Contents lists available at ScienceDirect

Computers and Fluids

journal homepage: www.elsevier.com

Three dimensionality in the wake of the flow around a circular cylinder at Reynolds number 5000

D.E. Aljure, O. Lehmkhul, I. Rodríguez, A. Oliva *

Heat and Mass Transfer Technological Center (CTTC), Universitat Politècnica de Catalunya BarcelonaTech (UPC), ESEIAAT, Colom 11, 08222, Terrassa, Barcelona, Spain

ARTICLE INFO

Article history:
Received 31 March 2016
Received in revised form 24 December 2016
Accepted 1 February 2017
Available online xxx

Keywords:
Direct numerical simulation
Coherent structures
Vortex shedding
Shear layer
Wake three-dimensionality
Vortex dislocations

ABSTRACT

The turbulent flow around a circular cylinder has been investigated at $Re = 5000$ using direct numerical simulations. Low frequency behavior, vortex undulation, vortex splitting, vortex dislocations and three dimensional flow within the wake were found to happen at this flow regime. In order to successfully capture the wake three dimensionality, different span-wise lengths were considered. It was found that a length $L_Z = 2\pi D$ was enough to capture this behavior, correctly predicting different aspects of the flow such as drag coefficient, Strouhal number and pressure and velocity distributions when compared to experimental values. Two instability mechanisms were found to coexist in the present case study: a global type instability originating in the shear layer, which shows a characteristic frequency, and a convective type instability that seems to be constantly present in the near wake. Characteristics of both types of instabilities are identified and discussed in detail. As suggested by Norberg, a resonance-type effect takes place in the vortex formation region, as the coexistence of both instability mechanisms result in distorted vortex tubes. However, vortex coherence is never lost within the wake.

1. Introduction

Aerodynamic research has been going on for over 100 years where bluff body flow has been a very active research area and the flow around a circular cylinder a benchmark problem. Flow over this geometry has been extensively studied and the understanding of the dynamics and structures present has grown extensively in the past few decades. Geometrical simplicity and an abundance of relevant three dimensional results make this an exceptional case study. Experimental observations on this geometrical configuration date back to the late XIX – early XX century with the work of famous physics like Strouhal, Von Kármán and Prandtl; and hundreds of research papers have been written concerning the study of the present configuration (see for instance Williamson [48] and citations therein).

The laminar to turbulent transition in the present case is limited by the particular geometry and flow conditions, i.e. transition is not induced by the body geometry itself but rather by the interactions of different unstable regions in the flow. Three different zones can be found: the boundary layer in the cylinder, two shear layers on top and bottom of the body and, finally, the wake. Extensive work carried out by different authors such as Bloor [2], Gerrard [8], Roshko [35], 36] have made possible the description of the different regimes encountered and the particular phenomena associated with them.

A number of experimental and numerical studies [49,29,39,40, amongst others] have been focused on the phenomenon of three-dimensional wake transition which occurs at Reynolds numbers between $Re = 190 - 260$ [48]. This regime has been associated with discontinuities in the Strouhal number and base pressure coefficient as the Reynolds number increases. Furthermore, the appearance of vortex pairs, vortex adhesion [49], upstream facing vortex loops [18] and low-frequency irregularities [2] have also been reported. This geometry and the three dimensional behavior present was further studied by Williamson [46], who observed an additional phenomenon: vortex dislocations. This phenomenon is related to the break down of turbulence and is considered as a mechanism of wake transition, as the vortex shedding shifts from wake mode A to wake mode B. Natural vortex dislocations have been also reported in different wake-type flows such as mixing layers [5], the flow over a flat plate [22], the flow over a cone [28] and the flow over a stepped cylinder [19]. Vortex dislocations might be seen as defects in the two dimensional vortex tubes whose continuity is broken as a consequence of the frequency difference between two span-wise cells [46] or between cells of similar frequency which are out-of-phase with each other [5]. Braza et al. [4] studied the natural vortex dislocation phenomenon that occurs in the three dimensional wake transition at $Re = 220$. They showed the existence of naturally occurring dislocations in the near wake, and the similarity of these structures to those obtained by Williamson [46] using a ring on the cylinder to force their appearance. Additionally, they analyzed the physical processes related to the introduction of stream and cross-stream-wise vorticity components and their impact on the span-wise variations of the Von Kármán vortex filaments and described the steps that lead to vortex dislocations.

* Corresponding author.
Email addresses: davidal@cttc.upc.edu (D.E. Aljure); oriol.lehmkuhl@bsc.es (O. Lehmkhul); ivette.rodriguez@upc.edu (I. Rodríguez); oliva@cttc.upc.edu, cttc@cttc.upc.edu (A. Oliva)

http://dx.doi.org/10.1016/j.compfluid.2017.02.004
0045-7930/

At higher Reynolds numbers, vortex irregularities have been suggested to be related with fundamental changes in the three-dimensionality of the wake past a cylinder. Several authors have observed transitional behavior around $Re \approx 5000$. This behavior is evidenced by different changes in wake configuration. An increase in the fluctuations of drag and lift forces and a loss of coherence in the vortex shedding (observed as a wider bandwidth in the spectrum at the vortex shedding frequency) have been reported. Furthermore, several authors point to changes in the base pressure profile and the vortex formation length, as well as, variation in length and behavior of the shear layers.

Son and Hanratty [38] studied the velocity gradients around the cylinder observing an increase in the separation angle with Reynolds number. Additionally they found that a small zone of positive velocity gradient, which they named zone B, appeared after the separation point and could be explained by the existence of a small separation bubble that decreased in size with Reynolds number. Finally, observations for the region following region B, region C (back of the cylinder), showed that for $Re = 5000$ and $Re = 10,000$ the gradient in this zone remains small with a slight increase towards the cylinder centerline, larger for Re =10,000. For Reynolds numbers $Re \geq 20,000$ the trend in the profile seemed to change with a much larger increasing rate as it approaches the cylinder center. The authors stated that results in this section are open to question due to the small magnitude of this quantity and that it may be changing direction. Kourta et al. [14] observed, through hot-wire measurements and flow visualizations, two different types of interaction between the vortex shedding and the small scale structures in the transition process in the cylinder wake. For a lower Reynolds range, that they defined as $2000 < Re < 16,000$, they found a strong interaction due to similar frequencies in both phenomena. For the larger Reynolds numbers, $16,000 < Re < 60,000$, the two phenomena are disconnected and the small vortices act as an eddy viscosity. Unal and Rockwell [43] found that the formation length decreased for Reynolds numbers $Re > 1900$, indicating an increase in the base pressure coefficient. Additionally for the higher Reynolds numbers they studied, $Re = 3400$ and $Re = 5040$, a distortion in the velocity fluctuation distribution with respect to the kinetic energy appeared, larger for $Re = 5040$. Finally, they performed an eigenfunction analysis on the velocity distribution along the shear layer and compared it with theoretical distributions finding that the data for Reynolds numbers between $1900 < Re < 3400$ follows the theory, however large deviations were observed for $Re = 5040$. Lin et al. [20] performed experimental observations on this geometry, observing for the Reynolds numbers $Re = 1000$ and $Re = 5000$ low levels of vorticity and low speed in the base region. They argued that the vortex formation is decoupled from the near-base region of the cylinder and this implied a predominant role of convective-type instabilities leading to large vortex formation. The authors wondered whether there is a shift in the vortex formation regime causing a change from the convective to a global instability mechanism for higher *Re* numbers and if this change in vortex formation mechanism is responsible for the large changes in the base pressure coefficient observed in the Reynolds number range $1000 < Re < 10,000$.

Norberg, in several works [23,24,26,27], showed the appearance of a transition in wake behavior for the flow at $Re \approx 5000$ including undulating vortex filaments and vortex splitting. He suggested that these structures might be related to what he observed as a shift from high to low quality vortex shedding. Finally, Norberg suggested that for $Re < 5000$ transition to turbulence is triggered by vortices in the wake, whereas after that *Re* number turbulence is triggered by a Kelvin–Helmholtz (KH) instability within the shear layer. At the critical value ($Re = 5000$) the two mechanisms coincide causing a resonance like behavior. Prasad and Williamson [31] investigated the changes in the three-dimensional near-wake structures over the time for $190 < Re < 10,000$ and the influence of the end conditions on the flow structure. The authors paid special attention to the wake transition regime and its relation with the flow parameters, including the vortex shedding frequency. They devoted especial attention to the flow around $Re \approx 5000$ where they stated the wake might be experiencing a fundamental change. They observed different phenomena such as a discontinuity in the value of the Strouhal number, a twin-peak spectrum near the vortex shedding frequency and vortex dislocations along the cylinder axis. The authors question whether these observations were introduced by the end plates used in their experiments, the finite length of the cylinder or if they were a real feature of the flow. Rajagopalan and Antonia [32] also studied the flow over a large range of Reynolds numbers in the sub critical range and focused on the shear layer instabilities. They found that the relation of the ratio between shear layer frequency and vortex shedding frequency with the Reynolds number changed around $Re = 5000$. This change supports the previous observations of a change in the flow organization at this *Re* number. Supporting the hypothesis proposed by Lin et al. [20], Rajagopalan and Antonia [32] suggested that a convective instability mechanism governs the flow for $Re > 5000$ rather than a global instability mechanism.

It is important to note that some scattering of results has been observed in this Reynolds number range, probably due to different experimental configurations (span-wise length, blocking ratio, time integration period, inflow conditions). However, the work done so far evidences the presence of a transition in wake behavior for the flow around $Re \approx 5000$. The present work aims to investigate this configuration using direct numerical simulations (DNS) in order to confirm the presence of the three dimensional behavior observed at $Re = 5000$ and to try to deepen the knowledge into the transitional behavior observed. Additionally, a detailed study into the instability mechanisms present in the flow is carried out. To the authors' knowledge no DNS studies have been performed at this Reynolds number.

2. Mathematical and numerical model

2.1. Governing equations and numerical method

In order to study the flow, the incompressible Navier–Stokes equations are solved:

$$\frac{\partial u_i}{\partial x_i} = 0 \tag{1}$$

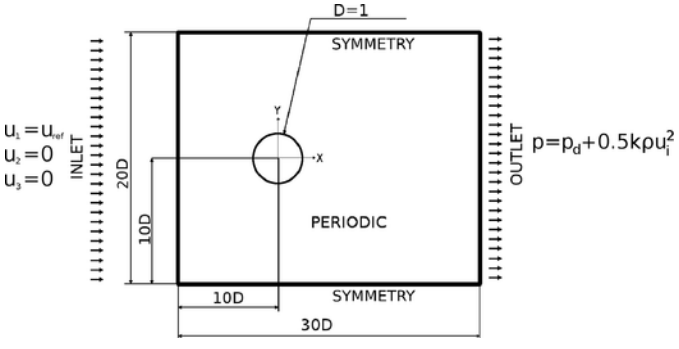

Fig. 1. Geometry and computational domain.

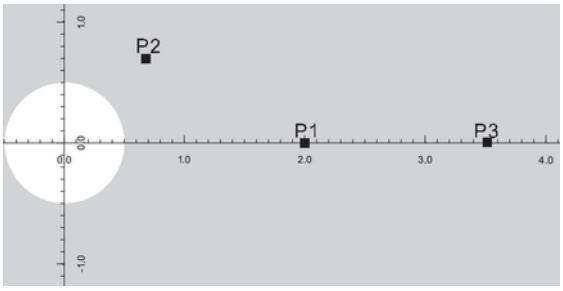

Fig. 2. Location of the computational probes, P1 $[x/D = 2\ y/D = 0]$, P2 $[x/D = 0.75\ y/D = 0.65]$ and P3 $[x/D = 3.5\ y/D = 0]$.

$$\frac{\partial u_i}{\partial t} + \frac{\partial\left(u_i u_j\right)}{\partial x_j} - \nu\frac{\partial^2 u_i}{\partial x_j \partial x_j} + \rho^{-1}\frac{\partial p}{\partial x_i} \quad = 0 \tag{2}$$

where u_i is the three-dimensional velocity field (u_1, u_2, and u_3 are also referred to as U, V and W), p is the pressure field, v stands for the kinematic viscosity and ρ for the density of the fluid.

A collocated unstructured mesh is built and the spatial discretization is carried out by means of finite volume techniques. A second-order conservative scheme [45] for the continuous differential operators, an explicit second order self-adaptive scheme for the temporal discretization, a back-ward Euler scheme for the pressure gradient and a fractional step algorithm for the velocity-pressure coupling are used. A more in depth presentation of the numerical schemes used can be found in Aljure et al. [1], Jofre et al. [11], Trias et al. [41]. As the meshes are constructed using a constant-step extrusion in the span wise direction of a 2D unstructured grid, the Poisson equation can be solved by means of a direct Schur-Fourier decomposition solver [3].

All simulations are run with the TermoFluids parallel unstructured code (www.termofluids.com) and are carried out on the in-house JFF cluster and on the Mare-nostrum III supercomputer, details on the computing characteristics are found in Aljure et al. [1]. METIS library [13] is used for domain partitioning and parallel communications are implemented following a pure distributed model by means of the Message Passing Interface (MPI) standard. Meshes reported in this work are partitioned from 160 to 512 CPUs, as meshes grow (see Table 1). The wall-clock time spent on each simulation is directly proportional to the number required of time-steps and their cost. For case M5, with a mesh of about 37×10^6 elements, the required iteration time is approximately 0.19 s on the Marenostrum supercomputer. For the whole simulation about 3.16×10^6 outer iterations are performed, which results in a simulation time of approximately 8.54×10^4 CPU hour. The code and numerical approach used in the present simulations have been proved to yield accurate solutions in flows with massive separations [1,16,17,33,34].

2.2. Definition of the case and boundary conditions

The geometry to be considered is a cylinder with diameter D shown in Fig. 1 submerged in an uniform fluid flow. Simulations are carried out at a Reynolds number $Re = U_{ref}D/\nu = 5000$ based on the cylinder diameter D and the free-stream velocity U_{ref}.

As this paper focuses on the three-dimensional effects that might appear in the near wake, three different span-wise sizes are considered: $Lz = n\pi D$, being $n = 1$, 2 and 3. Thus, the computational domain is $30D \times 20D \times Lz$ in the stream-, cross-stream and span-wise directions. The center of the cylinder is located at a distance of $10D$ downwind from the inlet boundary and at a distance of $20D$ from the outlet boundary (see Fig. 1).

A constant inlet velocity profile $u_i = \left(U_{ref}, 0, 0\right)$ is imposed. A pressure based condition is imposed for the outflow such that the mass conservation is fulfilled at each time step. In addition, in order to avoid any influence from non-physical waves reflected by the artificial outflow boundary, a buffer zone at $x > 14D$ is used [44]. Top and bottom surfaces are modeled as slip boundaries, periodic boundary conditions are set for the span-wise direction ones and the cylinder surface is modeled as a no-slip wall.

2.3. Computational domain and spatial discretization

In order to correctly solve all the phenomena present in the boundary layer a fine near wall mesh is necessary. Similarly, a fine mesh is also required for the full solution of the shear layers. Furthermore, the near wake zone must be refined to correctly predict the flow structures, i.e vortex shedding, Von–Kármán vortex street and three dimensionality. As the flow moves away from the cylinder the relative importance of flow structures in the force coefficients and velocity profiles diminish and so does the mesh resolution.

Details about the different meshes used are given in Table 1. The meshes used contain about 11, 23 and 34 million control volumes (CV) for πD, $2\pi D$ and $3\pi D$ span-wise lengths respectively for the 88,519 plane mesh. For the 115,709 plane mesh, they contain about

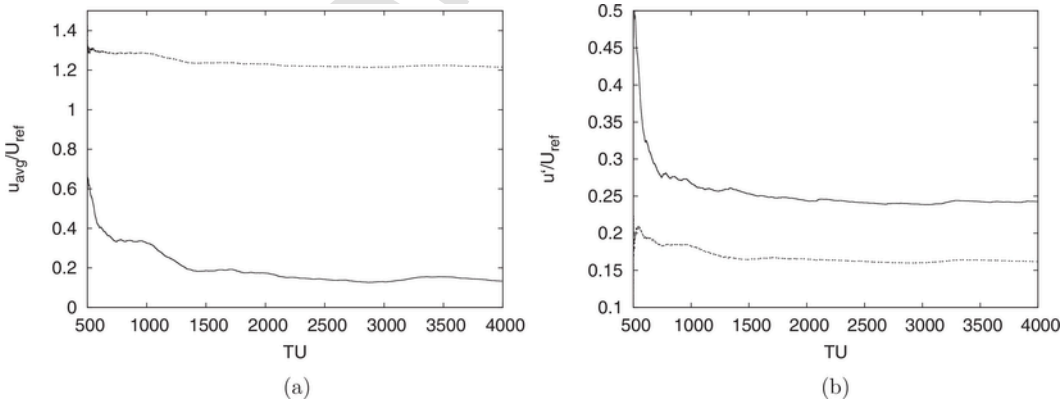

Fig. 3. (a): Time evolution of the averaged stream-wise velocity. (b): Time evolution of the stream-wise velocity fluctuations. Solid line: P1 [2D,0], Dashed line: P2: [0.75D,0.65D].

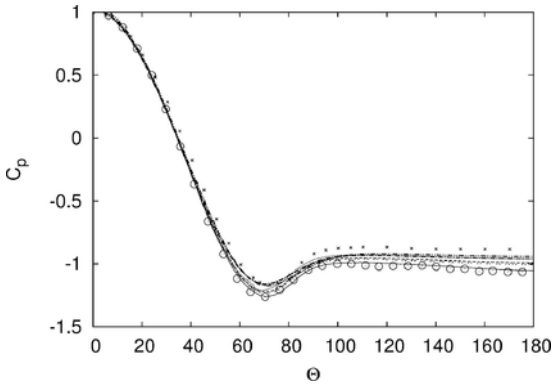

Fig. 4. Mean pressure distribution around the circular cylinder for the different meshes. Solid line mesh M1, dashed line mesh M2, dash-dash line mesh M3, dotted line mesh M4, dash-dot line mesh M5, dash-dot-dot Lehmkuhl et al. [17] ($Re = 3900$), crosses Norberg [26] ($Re = 3000$), circles Norberg [26] ($Re = 8000$).

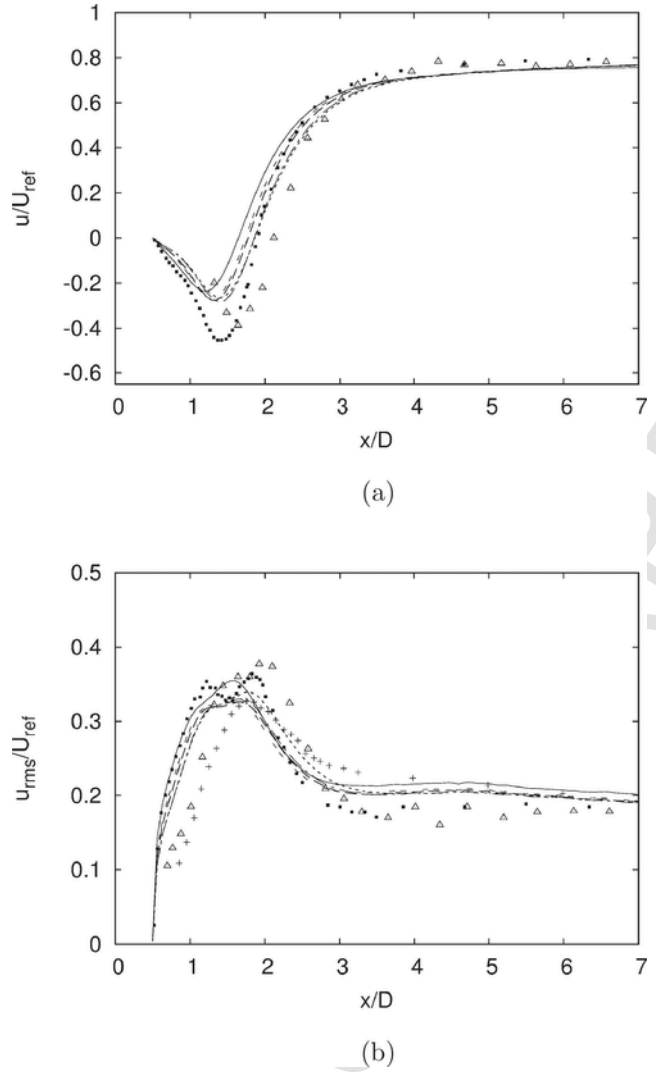

Fig. 5. Mean (a) stream-wise and (b) RMS stream-wise velocities in the wake center line. Solid line mesh M1, dashed line mesh M2, dash-dash line mesh M3, dotted line mesh M4, dash-dot line mesh M5, squares Norberg [26] ($Re = 5000$), triangles Lam et al. [15] ($Re = 6000$), crosses Prasad and Williamson [31] ($Re = 5427$).

18.6 and 37 million CV for πD and $2\pi D$ span-wise lengths, respectively.

2.4. Time integration study

Simulations are started from homogeneous flow and are advanced in time, about 500 time units ($TU = tU_{ref}/D$), until the initial transient behavior is washed out. Afterwards, statistics have been collected and averaged by integrating the instantaneous data over a sufficiently long-time period: about 3500 *TU*, over 700 shedding cycles. This time integration span results in a long simulation time and should ensure converged statistics and a large time span to analyze the three dimensional phenomena present. First and second order statistics are averaged in time and space (in the span wise direction). Flow magnitudes are also studied by means of probes in several locations (see Fig. 2). Fig. 3 shows the time history averaging for the first and second order statistics registered at different locations in the wake for mesh M5. Point 1 (P1) is located at the cylinder centerline, whereas Point 2 (P2) is located well within the shear layer. It can be seen in the figure that these quantities stabilize around $TU = 2000$ after being integrated for 1500 *TU*. A longer time integration span was chosen to fully guarantee well converged statistics along the whole domain.

2.5. Mesh sensitivity study

Although many meshes were used for computations, for the sake of brevity, results in this section are only presented for the meshes summarized in Section 2.3. In order to ensure that the smallest scales of the flow have been solved, a-posteriori analysis has been done by evaluating the ratio between the mesh size and the Kolmogorov scales. The latter are calculated using $\eta = \left(\nu^3/\epsilon\right)^{1/4}$, where ν corresponds to kinematic viscosity and $\epsilon = \nu S_{ij} S_{ij}$ the energy dissipation rate. Present simulations reach, for the finer meshes, a mesh ratio (h/η, being $h = \sqrt[3]{Vol_{cell}}$) under 3. The highest values found ($h/\eta > 3$) correspond to the shear and boundary layers, which are laminar and the Kolmogorov hypotheses do not apply. This parameter is especially important in the near wake area, that is $0.5 < x/D < 3$ and $-1 < y/D < 1$. Mesh M5 has, in this area, a volume-averaged ratio of resolved scales to Kolmogorov scales of $h/\eta = 1.1$. A second aspect to assess the meshes is the viscous boundary layer near the solid walls and its requirements to be well solved. In the case under study, the boundary layer is laminar, as transition to turbulence in the attached boundary layers occurs beyond $Re = 2 \times 10^5$ [36]. This fact allows the boundary layer thickness to be readily be estimated. The meshes used in this work are constructed so as to guarantee that at least 3 control volumes are located well within the boundary layer. Finally, the shear layers require a full resolution by having enough grid points within. Saad et al. [37] performed experiments to evaluate the behavior of the shear layer and the near wake of the circular cylinders. Their measurements in the unforced cylinder gave the approximate size of the shear layer for $Re = 5000$, 1.7478/*D* long and 0.2134/*D* wide. Considering this, over 5000 mesh points (for each plane) are located within this area to ensure its complete resolution.

In order to check the mesh discretization and grid parameters used in the present computations, results are compared to literature available results. In this sense, time-averaged flow parameters are summarized in Table 2. Studied magnitudes include the mean drag coefficient (C_D), the non-dimensional vortex shedding frequency (Strouhal number $St = f_{vs} D/U_{ref}$), base pressure coefficient ($-C_{p_{base}}$), fluctuating lift coefficient ($C_{L'}$), separation angle (ϕ_s) and recirculation length (L_{rec}/D). For comparison sake, values for these parameters are

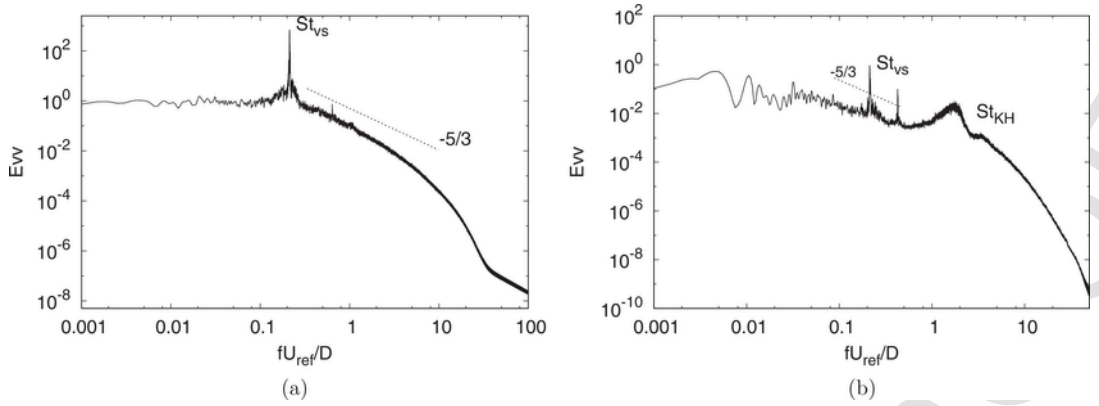

Fig. 6. Span wise averaged energy spectra of the cross-stream wise velocity fluctuations at two locations (a) P1 (b) P2.

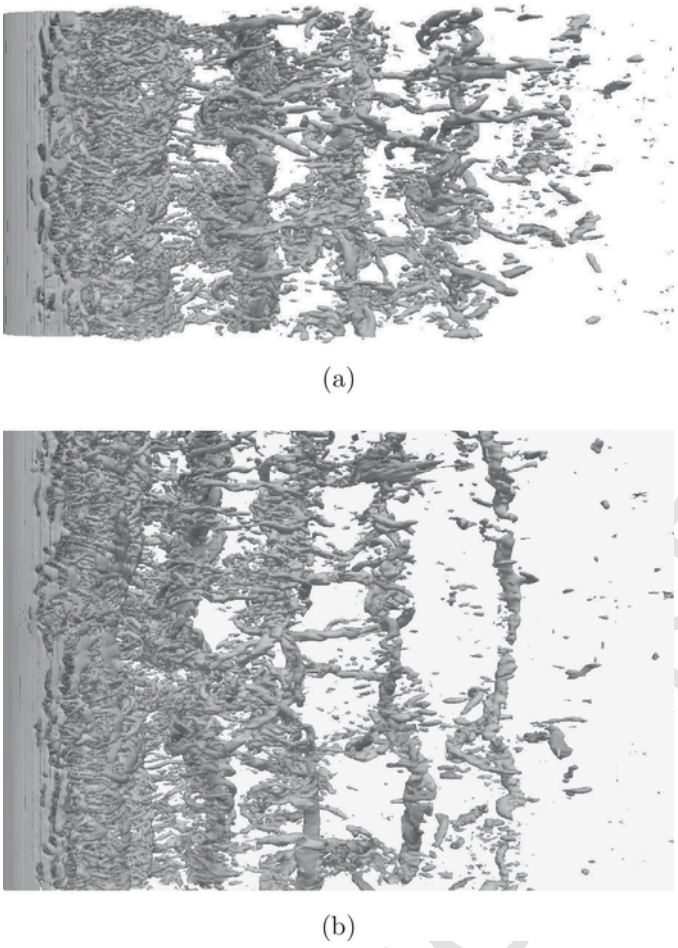

Fig. 7. Coherent structures represented by means of Q iso contours $Q^* = 3$. (a)$2\pi D$ span-wise length, (b) $3\pi D$ span-wise length.

presented from diverse published works (experimental and numerical) for the Reynolds number range $3900 \leq Re \leq 6000$. In general, computed parameters are in quite good agreement with published works, falling within the expected scattering reported at this Reynolds number. In particular present DNS results show minimal differences with the long-term solution by Lehmkuhl et al. [17].

Fig. 4 shows the mean pressure distribution around the cylinder. Results are compared to those measured by Norberg [24] for $Re = 3000$ and $Re = 8000$ and the long term averaged solution DNS

Table 1
Mesh parameters. CV_{plane} is the number of control volumes in the plane, N_{planes} is the number of planes in the span-wise direction, L_Z the length of the span-wise directions, NCV the total number of control volumes in the domain.

	CV_{plane}	N_{planes}	Δz	L_Z	NCV
M1		128		πD	1.13×10^7
M2	88519	256	$0.0245D$	$2\pi D$	2.27×10^7
M3		384		$3\pi D$	3.40×10^7
M4	115709	160	$0.0196D$	πD	1.86×10^7
M5		320		$2\pi D$	3.70×10^7

results by Lehmkuhl et al. [17] for $Re = 3900$. All results converge to the same curve for the laminar region of the boundary layer up to approximately 60°. After this position, solutions show small differences. Solution for mesh M5 and the long-term averaged solution for $Re = 3900$, again, show a similar behavior, however, pressure values are slightly lower for $Re = 5000$.

In Fig. 5, the stream wise velocity and its fluctuations in the wake centerline are plotted against results from the literature by Norberg [26] ($Re = 5000$), Lam et al. [15] ($Re = 6000$) and Prasad and Williamson [31] ($Re = 5427$). Results compare rather well, although main differences are present in the magnitude of the minimum velocity in the wake. As commented before, fundamental changes in the wake around this Reynolds number have been reported, affecting the wake topology and, thus, some scattering is expected. This is more evident in the stream wise velocity fluctuations, where different profiles around the maximum peak are observed. Norberg's averaged profiles resemble the low-energy mode (mode L) observed at $Re = 3900$ [17] with a two-lobed stream-wise velocity fluctuation profile and a lower stream-wise velocity minimum. Solutions obtained with all meshes showed a similar profile to that obtained for the long term solution at $Re = 3900$ by Lehmkuhl et al. [17]. In fact, the stream-wise fluctuation profile follows the same trend to that obtained by Prasad and Williamson [31] for $Re = 5427$. More results are presented in Aljure et al. [1].

Fig. 6 shows the energy spectrum of the cross-stream wise velocity fluctuations, and for comparison the $-5/3$ Kolmogorov law is also represented. Also, readily visible on Fig. 6a and b is the energy peak corresponding to the vortex shedding frequency, $St_{vs} = 0.21$, in agreement with literature reported results (see Table 2). In addition to the energy peak corresponding to the non-dimensional vortex shedding frequency, the KH shear layer instabilities non-dimensional frequency St_{KH} can also be seen on Fig. 6b as a broad-band peak around $St_{KH} = 1.65$. This broad-band peak energy peak is the result of an unstable shear layer that unevenly transports energy to the near wake. Flow in this geometry and with $Re = 5000$ shows a rather large vor-

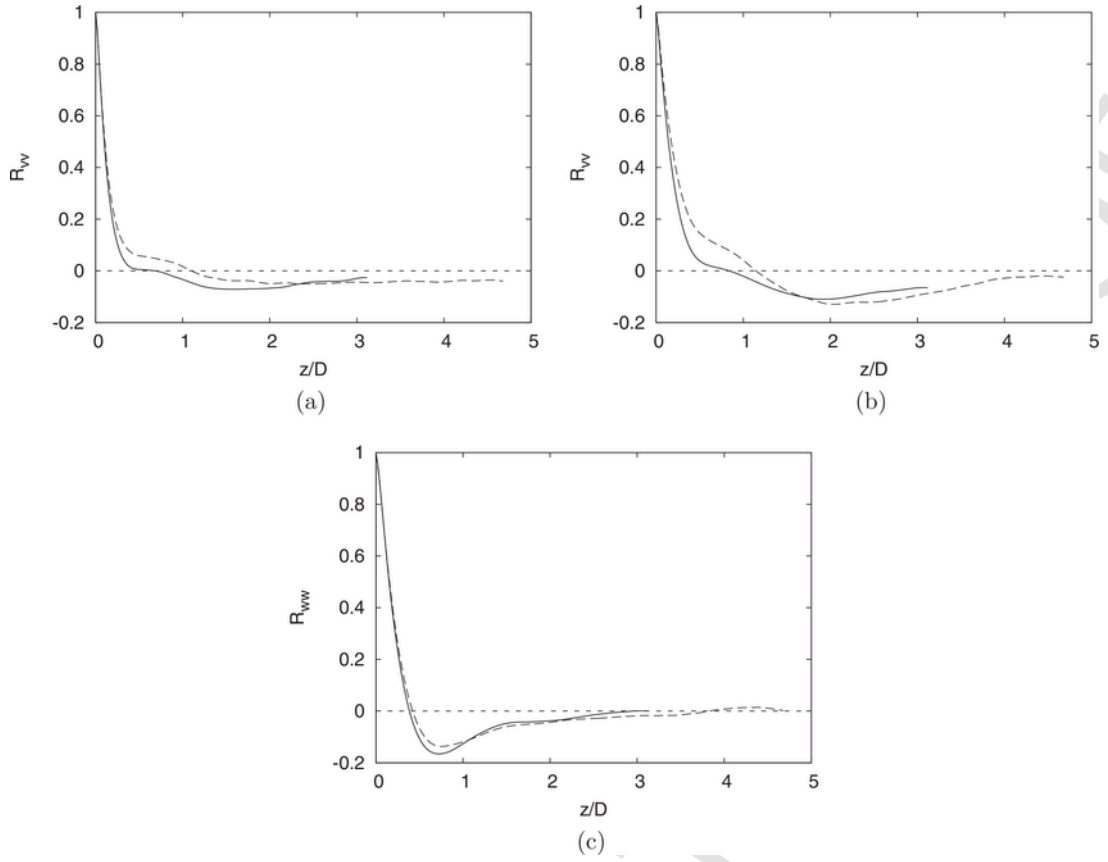

Fig. 8. Two point correlations in the span-wise direction for the velocity components. (a)Stream wise. (b) Cross-stream-wise. (c) Span wise. Solid line: $2\pi D$ span-wise length, Dashed line: $3\pi D$ span-wise length.

tex shedding peak evidencing a very energetic vortex shedding phenomenon. This large peak indicates a strong coherence in the flow and affects the rest of the spectrum showing harmonic peaks at higher wave numbers ($St \approx 0.42$ and $St \approx 0.63$). A harmonic peak is also present for the shear layer frequency around $St = 3.5$, although not as notorious as with the vortex shedding frequency. The frequency of these instabilities, which are closely related to the formation of vortices, has been measured experimentally by different researchers and its value expressed as a ratio of the vortex shedding frequency (St_{KH}/St_{vs}). Table 3 shows the present results compared to different results from the literature. The value of f_{KH}/f_{vs} found in the present work is within the range of these studies, where the ratio between these two frequencies varies from 6 to 8 for $Re \approx 5000$.

3. Results

3.1. Wake three-dimensionality

Proper identification of the vortical structures are a means for understanding the flow dynamics. In this work coherent structures are identified and analyzed by means of non-dimensional pressure iso countours $p^* = p/0.5\rho U_{ref}^2$, non-dimensional vorticity $\omega^* = \omega D/U_{ref}$ and non-dimensional Q-criterion $Q^* = QD^2/U_{ref}^2$ [10]. Fig. 7 shows, using the Q-criterion, the coherent structures using $2\pi D$ and $3\pi D$ span-wise lengths. It is important to point out that three dimensional behavior is seen in both domain lengths, having curved vortex cores and inclined vortex ribs. As the flow moves downstream, the span wise irregularities remain: vortex tubes show distortion and the span wise velocity component cause their shape to shift constantly. However, the span wise coherence of the vortex street is not lost.

As three dimensional behavior is observed in the wake, two point correlations are calculated to evaluate the span wise lengths simulated. Fig. 8 shows this parameter for the different velocity components at the location P1, also evidencing the footprint of span wise structures present in the near wake. Fig. 8a and c show that a span-wise length of $2\pi D$ captures correctly the three dimensional phenomena for the respective velocity components. Fig. 8b, which depicts the correlation for the cross-stream velocity, shows that the $3\pi D$ span-wise length is enough to correctly solve and capture the large scale span-wise behavior. The $2\pi D$ span-wise length captures this behavior, however it is cut short from returning to the zero value. As seen in Fig. 7, mesh M5 is able to capture the phenomena present, even though the span-wise length is $2\pi D$. Finally, it is important to point out that increasing the span-wise length from $2\pi D$ to $3\pi D$ carries with it a considerable increase in computational effort. Evidence of the three-dimensionality present in this configuration was presented by Norberg [24] for the flow at $Re = 5500$, and is shown in Fig. 9b. In the figure, a span-wise view of the flow obtained is presented (Fig. 9a) and compared to the flow visualizations made by Norberg [24]. The figure shows the undulating vortex filaments mentioned by Norberg [23], 24] and Prasad and Williamson [31]. Also seen in Fig. 9 is the vortex-splitting phenomenon, similar to a "Y" like shape in the near wake and marked in Fig. 9 for clarity. It is important to note the large length scale of the span-wise structures. A detailed study into three dimensional behavior in the wake is carried out in this section. To obtain an overall view of the vortex formation and the irregularities present Fig. 10 shows, using p^*, Q^* and ω^* iso sur-

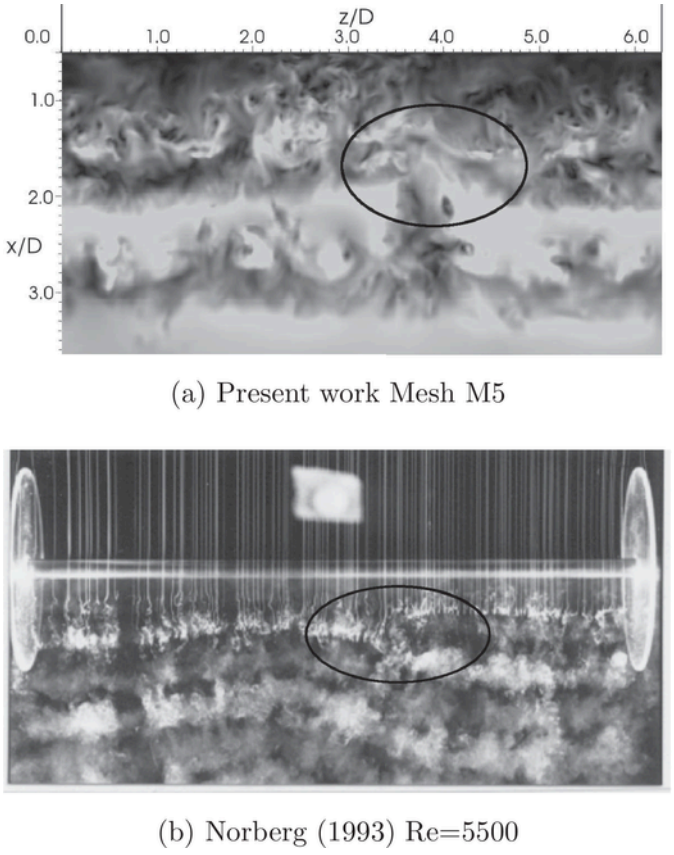

Fig. 9. Vortex dislocations, span-wise view. (a) Velocity field at the wake centerline plane. (b) Span wise flow visualization by Norberg at Re=5500 [24].

Table 2
Statistical flow parameters for the different meshes. Comparison with literature available results. Drag coefficient (C_D), Strouhal number (St), base pressure coefficient ($C_{p_{base}}$), fluctuating lift coefficient ($C_{L'}$), separation angle (ϕ_s) and recirculation length (L_{rec}/D). [a]: [24], [b]: [25], [c]: [27], [d]: [26].

Case	C_D	St	$-C_{p_{base}}$	$C_{L'}$	ϕ_s[°]	L_{rec}/D
colrule mesh M1	1.12	0.210	1.020	0.248	87.4	1.144
mesh M2	1.09	0.209	0.970	0.199	87.0	1.272
mesh M3	1.10	0.210	0.985	0.212	87.1	1.237
mesh M4	1.06	0.210	0.945	0.173	86.7	1.365
mesh M5	1.05	0.210	0.957	0.156	86.9	1.357
Norberg ($Re = 5000$ - EXP)	1.02[a]	0.209[a]	0.932[b]	0.146[c]	–	1.40[d]
Son and Hanratty [38] ($Re = 5000$ - EXP)	–	–	–	–	86	–
Lin et al. [20] ($Re = 5000$ - EXP)	–	–	0.84	–	–	–
Unal and Rockwell [42] ($Re = 5040$ - EXP)	–	–	0.84	–	–	–
Kourta et al. [14]($Re = 4800$ - EXP)	–	–	–	–	–	1.6
Jordan and Ragab [12] ($Re = 5600$ - LES)	1.01	0.206	1.02	–	87	–
Dong et al. [7] ($Re = 4000$ - EXP)	–	–	–	–	–	1.47
Lam et al. [15] ($Re = 6000$ - EXP)	0.96	–	–	–	–	1.62
Lehmkuhl et al. [17] ($Re = 3900$ - DNS)	1.015	0.215	0.935	–	88	1.36
Ma et al. [21] ($Re = 3900$ - DNS Case I)	0.96	0.203	0.96	–	–	1.12

faces, the events leading to the detachment of vortex tubes. At 1/8T, the top shear layer is starting to roll up creating a vortex core, named here Vt1. Additionally, marked in the image for clarity, flow structures from the bottom shear layer are seen to interact with the Vt1 vortex forming on top. As explained by Gerrard [8], entrainment flow is absorbed partially by the top shear layer and by the growing vortex, influencing the vortex formation. Entrainment flow towards the growing vortex does not vary significantly with Reynolds number, however, entrainment flow towards the opposing shear layer increases with increasing Reynolds number [8]. At the present flow regime, entrainment flow seems to affect the shear layer generating unstable behavior.

At 1/4T, the vortex Vt1 continues forming, however, irregularities that appear during the shear layer roll up create stream and cross-stream-wise structures that interact with the vortex core. These interactions modify their shape and the way they detach from the cylinder. Marked in the image are three locations that have been affected by these interactions.

At 3/8T, the uneven shear layer roll up ends up breaking the continuity in the structure of the vortex core. As the main vortex core starts to move downstream the locations marked in the image (same locations as in 1/4T) fall behind and remain attached to the vortex formation region.

At 1/2T, vortex Vt1 starts to detach from the formation region. As it does, it remains broken and the stream-wise structures interacting with it continue to deform the vortex core, see Fig. 10d. At this stage, parts of the vortex tube have already detached from the formation region, whereas some parts fall behind and remain attached.

At 5/8T, the detaching process is finished for all the span of the tube. As a result of the delayed locations identified in previous frames, several vortex distortions are visible and marked in Fig. 10e. Finally, at 3/4T, a second vortex tube (Vt2) starts to detach from the lower part of the cylinder. Entrainment flow is again visible leaving the top shear layer and entering the bottom shear layer and the vortex forming, so that the process is repeated. Additionally, vortex Vt1 is seen as it travels downstream taking part in the span wise coherent vortex street. Direct effects of the three dimensional behavior can be seen on the vortex cores as they travel downstream. Fig. 11 shows the non-dimensional pressure p^* iso surfaces in the wake of the cylinder and the cross-stream velocity in the mid plane. The vortex cores are visible from the top of the cylinder (x-z plane) and show a higher grade of three dimensional behavior not seen in flows with lower Re [17]. Flow at the present regime show span-wise distortions of the vortex tubes after they detach from the formation region due to the irregularities present within the shear layers. These irregular vortex tubes are then shed, and as they travel downstream their geometry continues to shift due to three dimensional phenomena present. It is interesting to note the appearance of a local break in the vortex tubes, similar to what has been described as vortex dislocations [4].

Vortex dislocations can be seen as a local break of the vortex tubes and have been considered a characteristic of the instability mode-A occurring at $Re \approx 200$ [47,48]. Furthermore, dislocations have been confirmed numerically by the DNS of Braza et al. [4], where they found that vortex dislocations in the transition regime were accompanied by a shift in phase of the mode A undulations. Their existence at $Re \approx 5000$ has also been experimentally observed by Prasad and Williamson [31], who documented the occurrence of dislocations along the span of the cylinder and raised the possibility that this phenomenon is a fundamental feature of the cylinder wake flow in the "upper-sub-critical regime" ($5000 < Re < 2 \times 10^5$). To confirm the presence of this phenomenon, time histories of velocity and pressure were analyzed. Fig. 12 shows, by means of the cross-

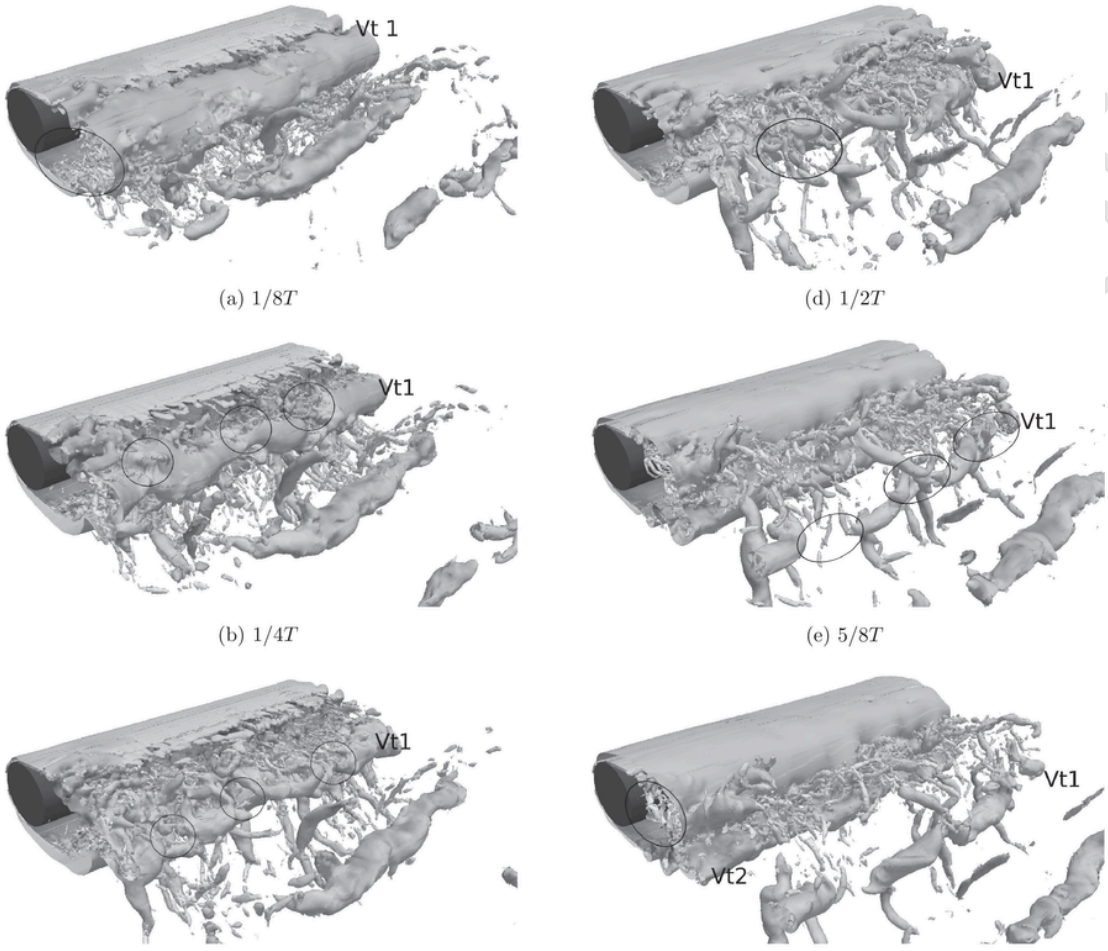

(a) $1/8T$ (d) $1/2T$

(b) $1/4T$ (e) $5/8T$

(c) $3/8T$ (f) $3/4T$

Fig. 10. cont: Vortex detachment time evolution. $p^* = -0.4\ \omega_z \pm 15$ and $Q^* = 50$ iso surfaces.

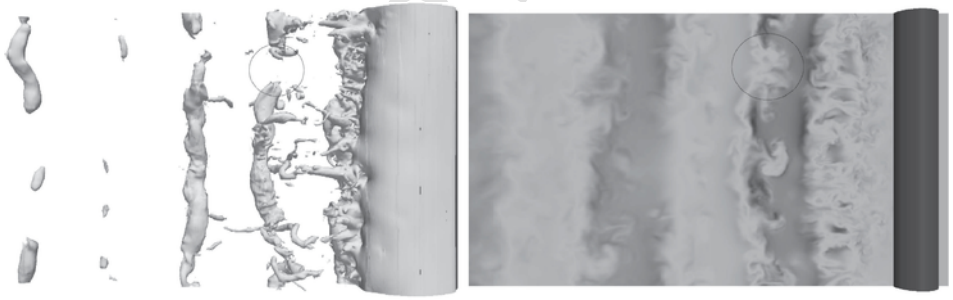

(a) (b)

Fig. 11. (a) $p^* = -0.7$ iso surface and (b) Cross stream velocity in the mid plane showing the loss of coherence in a vortex tube.

stream velocity and pressure time history, the presence of what might be vortex dislocations. The velocity signal shows modulation, whereas the pressure signal shows a local maximum, followed by a rapid drop. Both features suggests a dislocation is passing through (both events are marked in the images for clarity). It is interesting to provide an overall view on the effect of vortex distortions observed on the wake flow. Fig. 13 shows the passage of different vortex tubes by means of the cross-stream (V/U_{ref}) velocity time history. First, and most notorious, at location P1 a large number of distortions are visible (Fig. 13a). Moreover, the local breaks in the vortex tube continuity throughout the span seem to show a random distribution with time. As has been shown in Fig. 6, the shear layer instability shows a broad-band characteristic frequency, whereas no characteristic frequency has been found for the convective-type instability. This behavior suggests the convective instability is constantly present within the near wake, whereas the shear layer instability occurs at different moments in time and span wise location. The appearance of the shear layer instabilities might be causing, as suggested by Norberg, a reso-

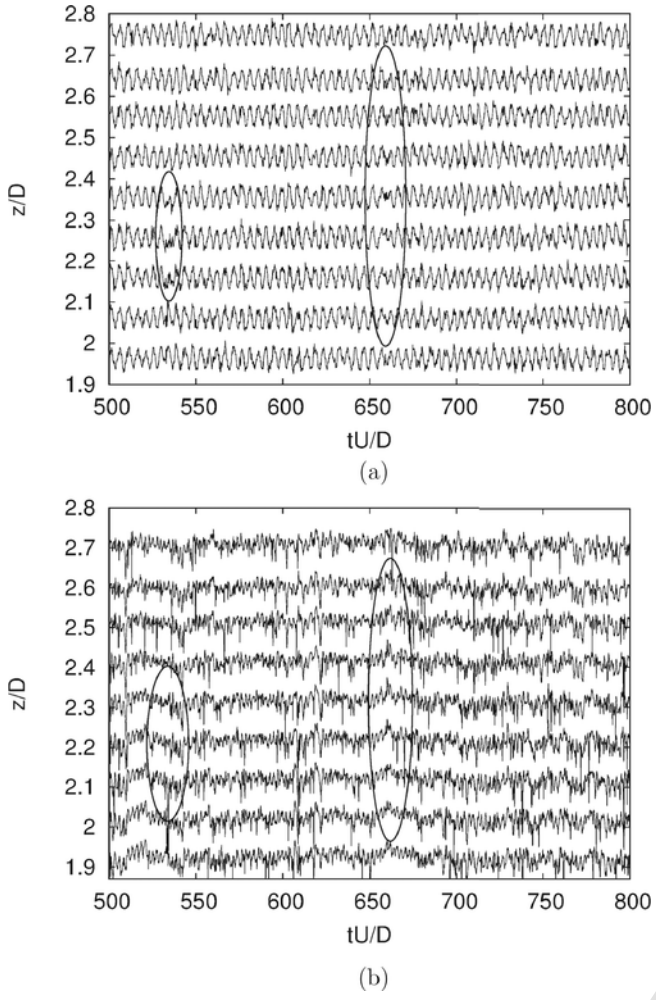

Fig. 12. (a) Cross stream velocity and (b) pressure time history for P1 showing the passage of a vortex distortion.

nance type effect that distorts the shear layer roll-up. A detailed analysis showing the steps leading to vortex distortions is carried out in Section 3.3. Local discontinuities are visible on almost all vortex tubes shown in Fig. 13a, and no direct relation can be observed between the dislocations in adjacent vortex cores. Fig. 13b shows the cross-stream velocity at a location further downstream, P3. At this location barely any distortions are seen on the vortex tubes. The DNS study by Braza et al. [4] concluded that the appearance of stream wise vorticity in the cylinder wake, led to the appearance of vortex dislocations which affected the coherence of the whole wake. However, this is not the case for the present flow regime.

3.2. Frequency analysis

In order to further study the behavior of the vortex shedding and KH instabilities in the near wake, a fast Fourier transform was performed on the cross flow velocity for each plane on P1 (see Fig. 2). The results are presented in Fig. 14. The vortex shedding frequency is seen as the dominant one in the flow for all z positions and, even though there are some variations in the spectral energy along the span, no large reduction of these energy peaks is observed at any span wise location. According to Braza et al. [4] spectral energy reduces in the regions where vortex dislocations occur, however, as observed in Fig. 14, spectral energy does not vary much along the span. This behavior suggests that the distortions do not affect the vortex shedding as their occurrence do not greatly change the energy associated with this phenomenon. To perform a more in depth study of the vortex shedding phenomenon present, a Fourier spectrogram for the cross flow velocity for the span wise mid plane is presented in Fig. 15. A spectrogram is a visual representation of the spectrum of frequencies in a signal as they vary with time. Results for this spectrogram are approximate due to the fact that present results are not evenly spaced in time. As expected, there is a high energy area around the non-dimensional frequency $St = 0.2$, coinciding with the vortex shedding frequency. Notice that even though the largest energy content occurs around the vortex shedding frequency, small variations in both frequency and energy are observed along the whole time span. These variations might be associated with irregularities in the vortex formation at that location. Close-ups of these variations are depicted in Fig. 15b–c for $1920 \leq TU \leq 2180$ and $2920 \leq TU \leq 3180$, where variations of the energy content and in the value of the vortex shedding frequency are shown.

As our data is unevenly spaced in time, and as seen from the spectrogram, several frequency components seem to be acting in the flow,

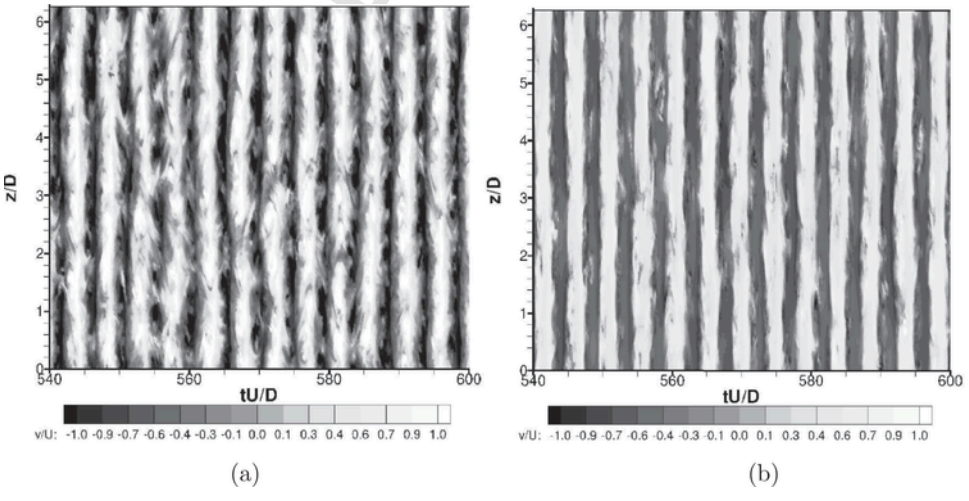

Fig. 13. Cross-stream velocity on the (t,z) plane, illustrating the local perturbations on the coherence of the signal at P1 (a) and the recovery of coherence downstream at P3 (b).

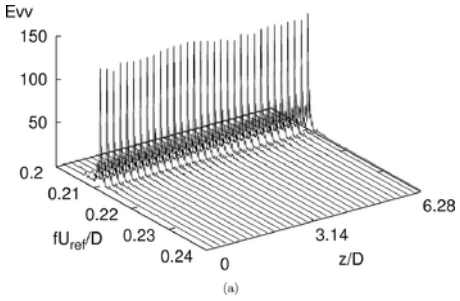

Fig. 14. Span wise variations of the energy spectra for the cross flow velocity for P1.

Table 3
Relation between shear layer frequency St_{KH} and vortex shedding frequency St_{vs}.

Author	St_{KH}/St_{vs}
Bloor [2]	7.95
Unal and Rockwell [42]	8.0
Chyu et al. [6]	6.7
Prasad and Williamson [30]	7.1
Present	7.86

the empirical mode decomposition (EMD) method proposed by Huang et al. [9] is here used. This method breaks down a signal into different function components, known as intrinsic mode functions (IMFs), and a monotone residue. This process is carried out by means of an iterative algorithm. The advantage of this method over others, such as the Fourier transform or wavelet analysis, is that data can be unevenly spaced, have non-linear behavior and be non-stationary. Thus, it renders the possibility of characterization and parametrization of multi-scale patterns.

This technique has been applied to analyze the signal of the cross-stream velocity of probe P1. As the probes used are sampled for all planes in the span wise direction, resulting in a N plane signal, the signal corresponding to the mid-plane has been used. For the analysis, the initial time-series has been decomposed into eight IMFs plus a residual. Fig. 16 shows the resulting decomposition. Observing the different IMFs it can be seen that the behavior in the present case is composed, as expected, of different frequency components. As can be observed from Fig. 16, each IMF component shows a lower frequency than the previous one. IMF 1 depicts the turbulent fluctuations inherent of all turbulent flows, whereas IMF 2 shows the vortex shedding component of the signal. As can be seen from this IMF component, vortex shedding shows irregularities in its frequency and amplitude with regards to time. The rest of the IMFs then represent the lower frequency components acting on the wake flow and introducing irregularities into the vortex shedding.

The Hilbert transform is then applied to each IMF to compose the Hilbert spectrum (Fig. 17), which presents a quantification of the energy and frequency variations in time. Observing the Hilbert spectrum in Fig. 17, the vortex shedding (high energy) phenomena is readily seen around the non-dimensional frequency $St = 0.2$. Additionally, the lower frequency components represented by the higher order IMFs are also seen, presenting an energy level comparable to

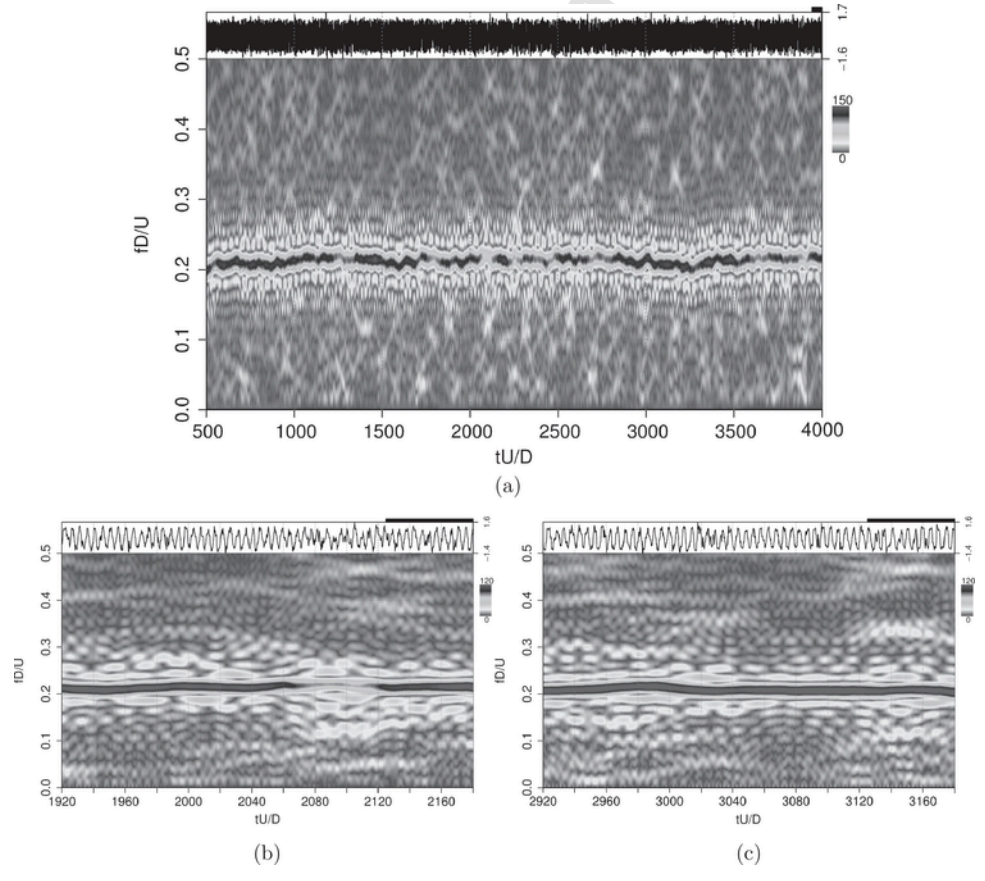

Fig. 15. Fourier spectrogram for the cross flow velocity for P1 at plane $z/D = \pi$. (a) All integration time. (b) close up for $1920 \leq TU \leq 2180$. (c) close up for $2920 \leq TU \leq 3180$.

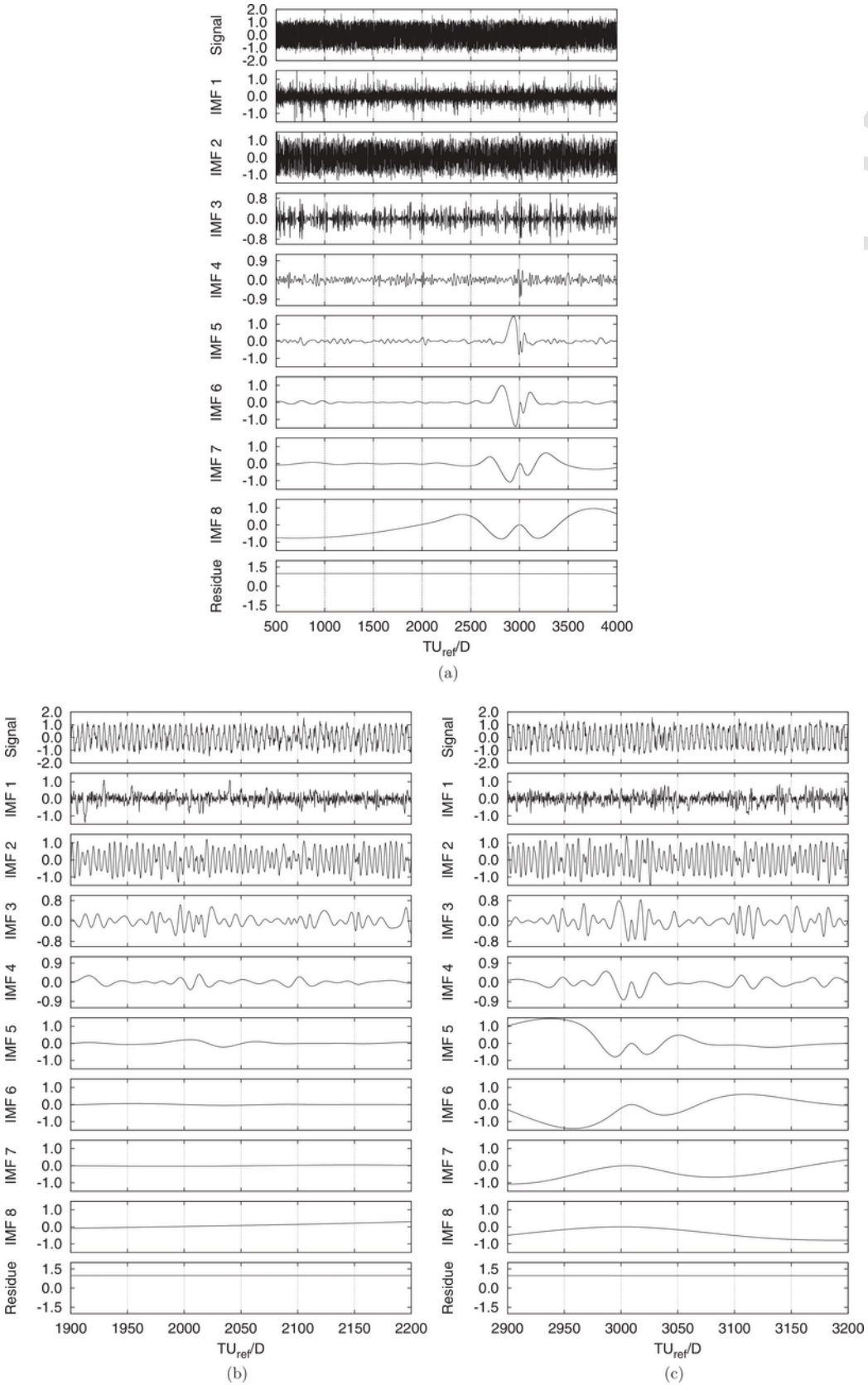

Fig. 16. Empirical mode decomposition of the cross flow velocity for P1 (a) full time range, (b) close up to $1900 \leq TU \leq 2200$, (c) close up to $2900 \leq TU \leq 3200$.

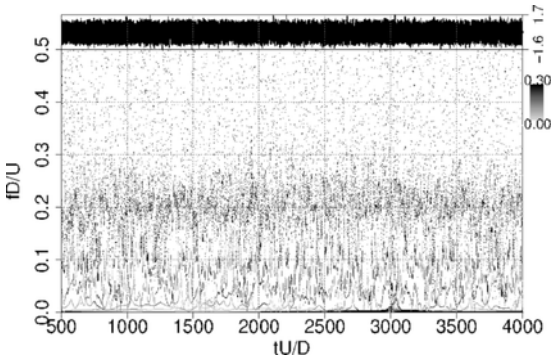

Fig. 17. Hilbert spectrum for the IMFs shown in Fig. 16. The energy levels increase as color darkens.

that of the vortex shedding. Interactions between these different frequencies disturb the local structure of the vortex street creating the 3D behavior observed.

3.3. Shear layers and instability mechanisms

Lin et al. [20], Norberg [26] and Rajagopalan and Antonia [32] all have suggested the existence of two instability mechanism in the wake of cylinders. Lin et al. [20] and Rajagopalan and Antonia [32] both have suggested the flow at the present Reynolds number is governed by a convective instability mechanism, i.e. instabilities stemming from the near wake, rather than by a global instability, i.e. instabilities in the shear layer. On the other hand, Norberg [26] suggests that the two instability mechanisms coincide for $Re = 5000$ causing a resonance like behavior.

Fig. 18 shows, for the same time instant, a span wise view at two different planes where the vortex formation structure varies as the flow is governed by the different instabilities. As the shear layer instability occurs transition to turbulence takes place in this region. On the contrary, when the flow is governed by the convective type instabilities transition is done within the recirculation zone, resulting in a larger vortex formation region. The co-existence of these two types of instabilities result in the un-even shear layer roll up observed in Fig. 19.

The shear layer roll up defines how the vortex tubes are formed. Fig. 19a shows the shear layer roll up at $TU = 2500.6$. Shear layers are visualized using non-dimensional span wise vorticity at a level 5.5% of the maximum span wise vorticity on the cylinder surface (defined in a similar fashion as in Dong et al. [7]). Marked in the image are locations where the shear layer roll-up evidences the span wise irregularities in its length. Fig. 19b shows the resulting vortex tube at $TU = 2503.6$. Marked in the image are the locations where the 2D continuity of the tubes is disrupted. Also, note there exists more than one location where the continuity is lost along the span.

To further study this behavior, span wise velocity is plotted over time at two different span wise locations, $z/D = 2.2$ and $z/D = 4.1$. As can be seen in Fig. 20, the shear layer shows the KH instability for $z/D = 4.1$, whereas it is not present in span wise location $z/D = 2.2$.

To further understand the vortex irregularities generated, Fig. 21 shows, using non-dimensional Q ($0 \leq Q^* \leq 50$) and pressure ($-0.3 < p^* < -2$) contours, the vortex detachment process on two different span-wise planes for a vortex shedding cycle around $TU = 2500$. Fig. 21a shows the first step in this process where, as the shear layer finish their roll up phase, the vortex tube starts to move downstream. Notice in the left of Fig. 21a, the large amount of small structures (shown as the darker contour) in the vortex formation region compared to those present in the right. It is also important to notice the slightly larger formation length present in the left.

As time advances, the vortex core starts to detach (Fig. 21b), however, the influence of the different mechanisms present cause vortex detachment to be done in a different fashion. In the left of Fig. 21b, the vortex core moves downstream as it detaches from the recirculation area. However, in the right of the image, the vortex core starts to deform as the shear layer delays the vortex detachment, as seen in the right of Fig. 21b.

In the later stages of vortex detachment (Fig. 21c), the vortex tube (on the left side) successfully detaches and starts to travel downstream maintaining its circle-like shape. In the right, pressure contours deform greatly as the vortex core detaches. In this plane the structural integrity of the span-wise structure is lost, however, the span wise coherence is recovered downstream, as seen in Fig. 21d.

At a vortex shedding cycle around $TU = 2513$, the vortex tubes do not show the large deformations visible in Fig. 19b (see Fig. 22b). As the shear layer rolls up to create this vortex tube, it does so without the large span wise irregularities in its length (see Fig. 22a). In a similar fashion as before, the span wise velocity is plotted for the two span wise locations $z/D = 4.8$ and $z/D = 1.8$ in Fig. 23. A quick examination reveals that no shear layer instabilities are present in these planes, suggesting this vortex tube is completely governed by the recirculation instability mechanism.

Fig. 24 shows, similarly as Fig. 21, the vortex detachment process at the two span wise locations shown in Fig. 23. The beginning of this process is similar to what was observed before. Fig. 24a, shows the small structures within the recirculation area. Note that the vortex formation length is slightly different, however, the vortex in the right is larger.

As the shear layer roll up finishes, the vortex tube starts to move downstream, and it does so in a more uniform fashion than that ob-

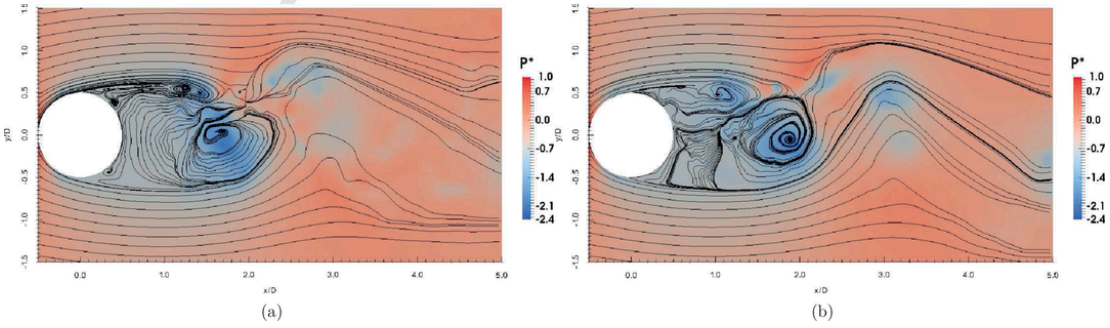

Fig. 18. Span wise view at two locations showing the two different types of instabilities governing the flow, (a) $z/D = 5.89$ global instabilities and (b) $z/D = 0.2$ convective instabilities. Figure is colored by pressure.

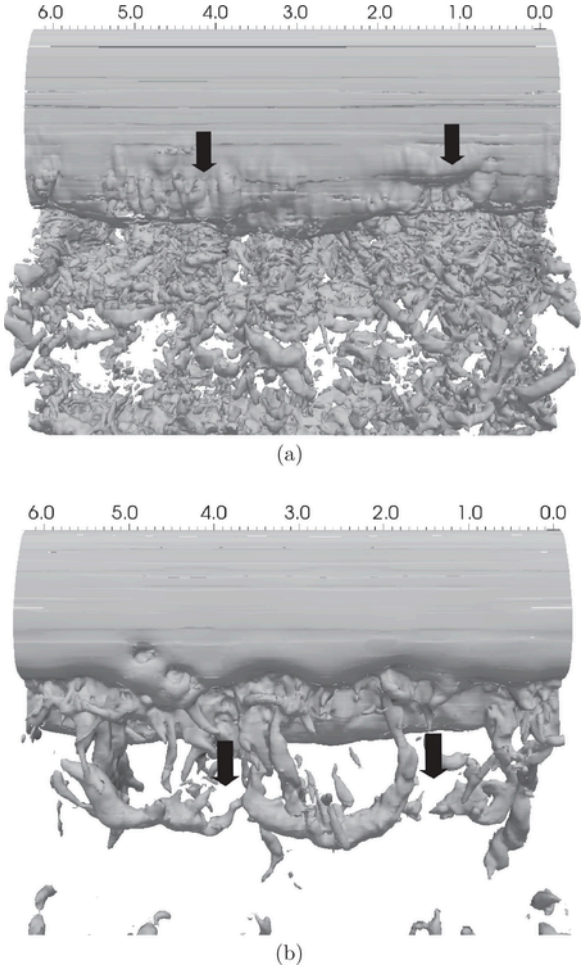

Fig. 19. Shear layer roll up for (a) $TU = 2500.6$, using span wise non-dimensional vorticity $\omega_z^*/\omega_{z-max}^* = 5.5\%$, and resulting vortex tubes (b) $TU = 2503.6$ using non-dimensional pressure $p^* = -0.7$. Both images are colored by span wise velocity.

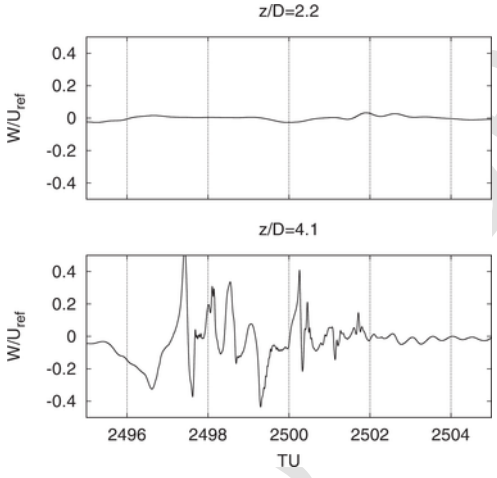

Fig. 20. Span wise velocity within the shear layer (P1) at two span wise locations, $z/D = 2.2$ and $z/D = 4.1$.

served in Fig. 21 (see Fig. 24b). It is important to note that the cross-flow location of the vortex center varies along the span. Finally, Fig. 24c–d show the vortex tube as it finishes the detachment process and travels downstream. The structural integrity of this tube is conserved throughout the whole process and the resulting vortex tube has a quasi-2D structure (Fig. 22b).

4. Conclusions

DNS computations were carried out to study the flow around a circular cylinder at $Re = 5000$. Different authors point to this flow regime as a transition point in the flow behavior. In order to correctly capture the three dimensional behavior found in this flow regime, a larger span-wise size than that used for previous DNS with lower *Re* had to be used. In the present investigation a span-wise size of $2\pi D$ was found to be enough to capture the three dimensional phenomena. In general, results from the present simulations agree quite well with published works, falling within the expected scattering present at this Reynolds number. The long-term solutions performed along 3500 *TU* show a similar profile to that observed for $Re = 3900$ [17]. As expected, vortex shedding and KH instabilities are observed and large energy peaks are obtained in the energy spectra indicating a very coherent vortex shedding and a strong influence of the KH instabilities in the rest of the flow.

For this flow regime, the shear layers and the near wake exhibit a three-dimensional behavior not observed at lower Re numbers, which points out to a fundamental change in the flow. The three-dimensionality of the wake is seen as vortex distortions and variation in the vortex formation length. The latter, was already reported at a lower Reynolds number of $Re = 3900$ [17]. However, at $Re = 5000$, the three-dimensional behavior is extended to the whole near wake region exhibiting vortex splitting, vortex undulation and local vortex dislocations. In contrast to the vortex dislocation reported by Braza et al. [4], all these phenomena are found to be limited to the vortex formation region, as the coherence of the vortex street is not lost downstream.

As previously suggested by Norberg, it has been found evidence that the three-dimensional behavior appears to be the result of the coexistence of two instability mechanisms: a global and a convective-type instability. Actually, Norberg suggested that wake three-dimensionality is caused by a resonance-like behavior within the near wake. Present results show evidence that the resonance effects does exist, and the three dimensional behavior is triggered by the occurrence of both global and convective, instabilities within the same vortex tube. These two instabilities at a same span wise location result in a different formation length and a distorted shear layer. As the shear layer roll up happens, vortex formation length variations in the span wise direction produce distorted vortex tubes. Nonetheless, the span wise distribution of the local breaks in the vortex tubes shows a random behavior, and is related to the appearance of the shear layer instability.

Acknowledgments

This work has been partially financially supported by the "Ministerio de Economía y Competitividad, Secretaría de Estado de Investigación, Desarrollo e Innovación", Spain (project ref. ENE2014-60577-R), by the collaboration project between "Universitat Politècnica de Catalunya" and Termo Fluids S.L., a PDJ 2014 Grant by AGAUR (Generalitat de Catalunya), and by the "Departamento Administrativo de Ciencia, Tecnología e Innovación - Colciencias" via their doctoral training program "Francisco Jose de Caldas". We also acknowledge the access to MareNostrum SuperComputer III granted by the "Red Española de Supercomputación"

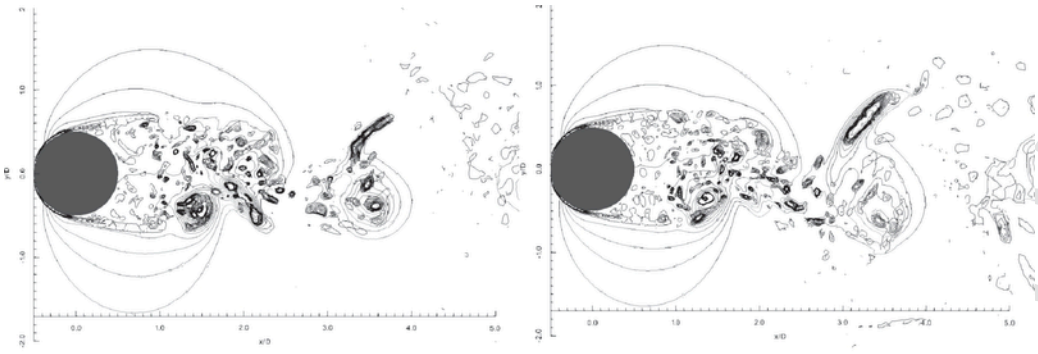

(a) $1/4T$

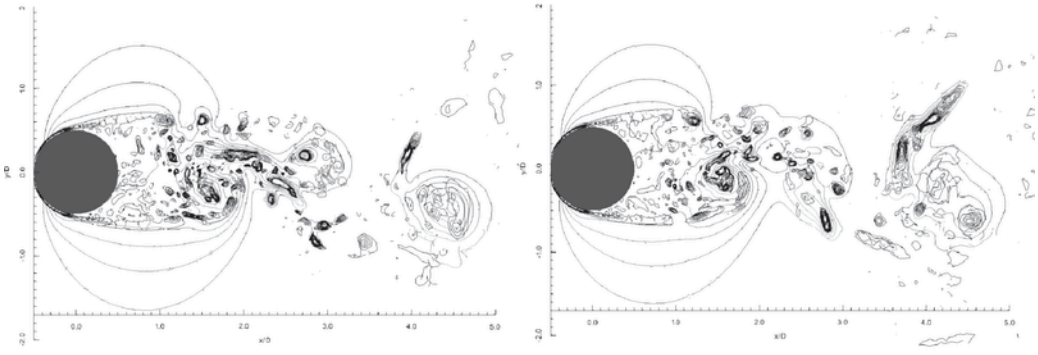

(b) $1/2T$

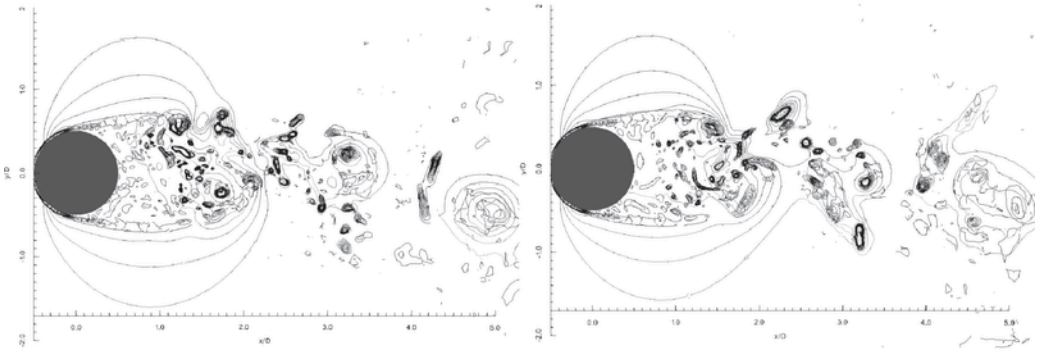

(c) $5/8T$

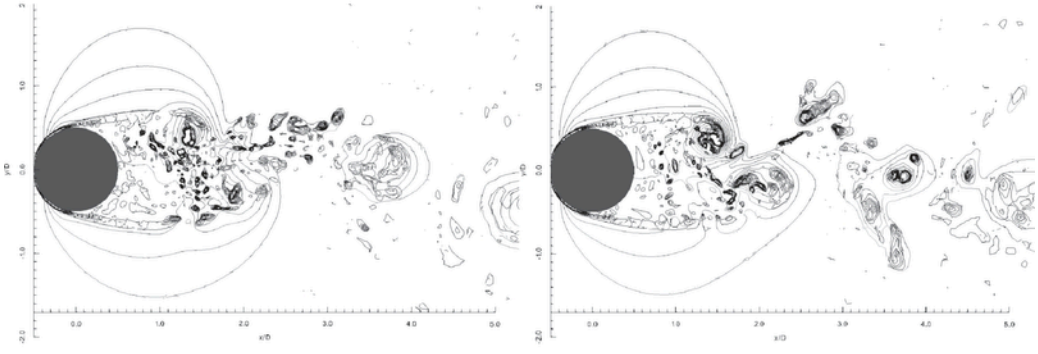

(d) $3/4T$

Fig. 21. Pressure and Q* contours depicting the shear layer roll up at two span wise locations, left $z/D = 2.3$ and right $z/D = 4.1$.

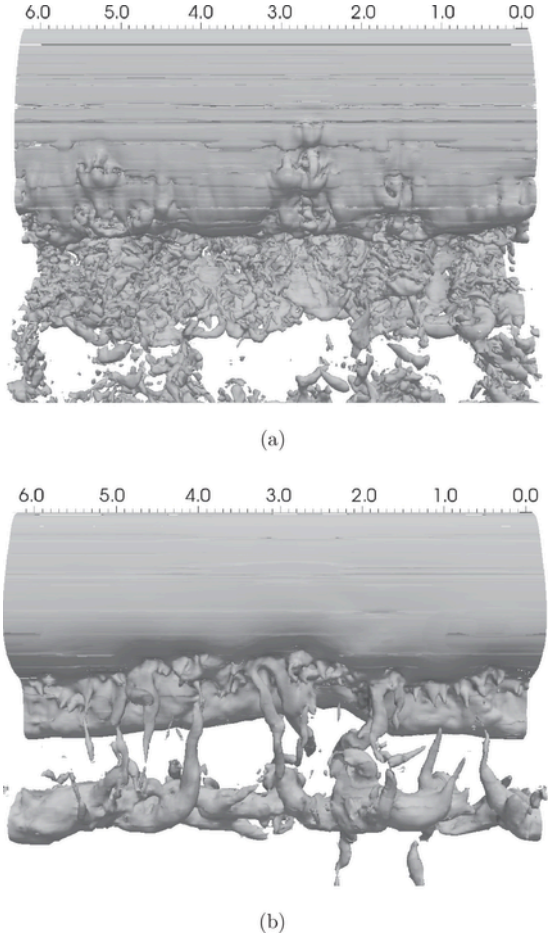

Fig. 22. Shear layer roll up for (a) $TU = 2513.1$, using span wise non-dimensional vorticity $\omega_z^*/\omega_{z-max}^* = 5.5\%$, and resulting vortex tubes (b) $TU = 2516.1$ using non-dimensional pressure $p^* = -0.7$. Both images are colored by span wise velocity.

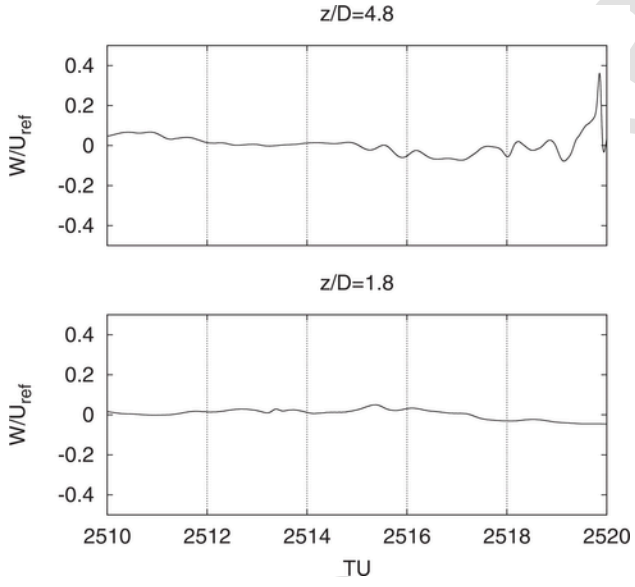

Fig. 23. Span wise velocity within the shear layer (P1) at two span wise locations, $z/D = 4.8$ and $z/D = 1.8$.

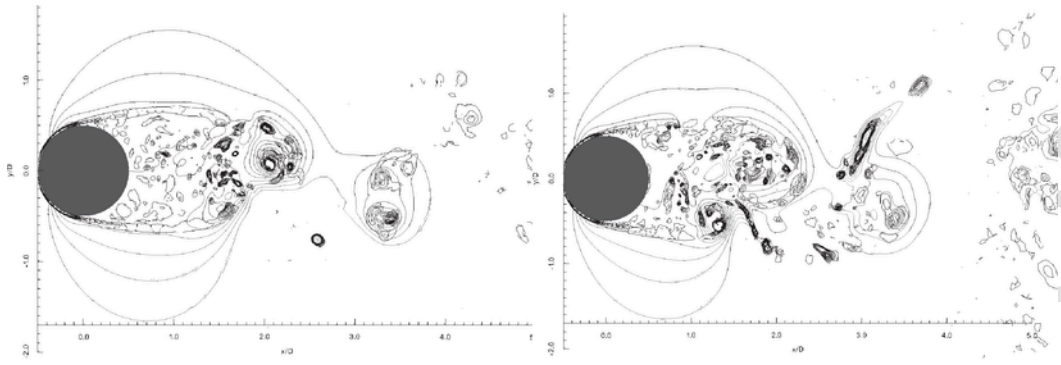

(a) $1/4T$

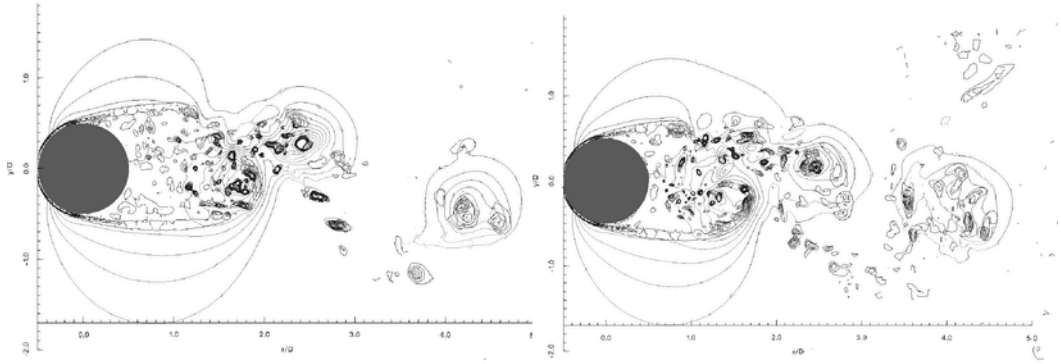

(b) $1/2T$

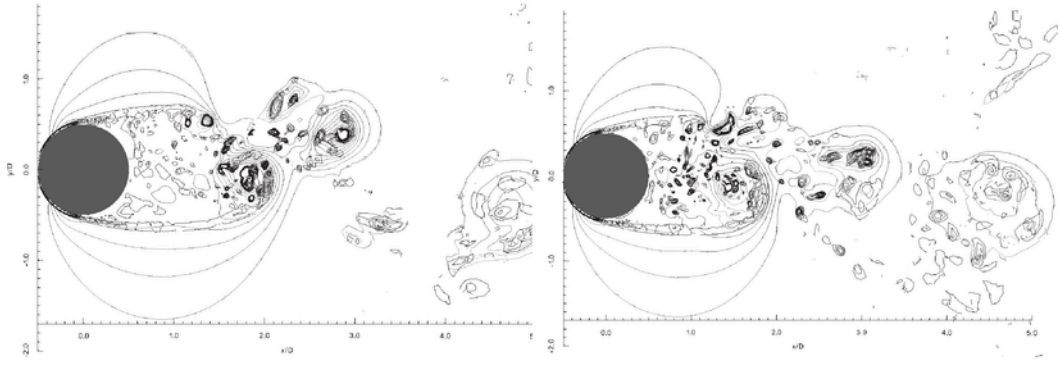

(c) $5/8T$

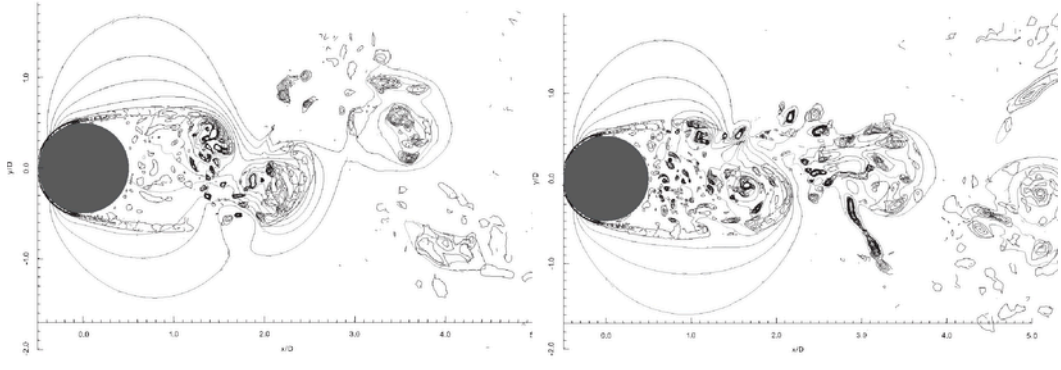

(d) $3/4T$

Fig. 24. Pressure and Q* contours depicting the shear layer roll up at two span wise locations, left $z/D = 4.8$ and right $z/D = 1.8$.

References

[1] D.E. Aljure, I. Rodríguez, O. Lehmkuhl, P.-S.C. D., A. Oliva, Influence of rotation on the flow over a cylinder at Re = 5000, Int J Heat Fluid Fl 55 (2015) 76–90.

[2] M.S. Bloor, The transition to turbulence in the wake of a circular cylinder, J Fluid Mech 19 (2) (1964) 290–304.

[3] R. Borrell, O. Lehmkuhl, F.X. Trias, A. Oliva, Parallel direct Poisson solver for discretisations with one Fourier diagonalisable direction, J Comput Phys 230 (12) (2011) 4723–4741.

[4] M. Braza, D. Faghani, H. Persillon, Succesive stages and the role of natural vortex dislocations in three-dimensional wake transition, J Fluid Mech 439 (1) (2001) 1–41.

[5] F.K. Browand, T.R. Troutt, The turbulent mixing layer: geometry of large vortices., J Fluid Mech 158 (1985) 489–509.

[6] C. Chyu, J.C. Lin, D. Rockwell, Kármán vortex formation from a cylinder: role of phase-locked Kelvin–Helmholtz vortices, Phys Fluids 7 (9) (1995) 2288–2290.

[7] S. Dong, G.E. Karniadakis, A. Ekmekci, D. Rockwell, A combined direct numerical simulation particle image velocimetry study of the turbulent near wake, J Fluid Mech 569 (9) (2006) 185–207.

[8] J.H. Gerrard, The mechanics of the formation region of vortices behind bluff bodies, J Fluid Mech 25 (2) (1966) 401–413.

[9] N.E. Huang, Z. Shen, S.R. Long, M.C. Wu, H.H. Shih, Q. Zheng, N.-C. Yen, et al., The empirical mode decomposition and the Hilbert spectrum for non-linear and non-stationary time series analysis., Proc R Soc Lond A 454 (903) (1998).

[10] J.C.R. Hunt, A.A. Wray, P. Moin, Eddies, stream and convergence zones in turbulent flows, Proceedings of the summer program 1988, 1988.

[11] L. Jofre, O. Lehmkuhl, J. Ventosa, F.X. Trias, A. Oliva, Conservation properties of unstructured finite-volume mesh schemes for the Navier–Stokes equations, Numer Heat Tr B-Fund 64 (1) (2014) 53–79.

[12] S. Jordan, S.A. Ragab, A large-eddy simulation of the near wake of a circular cylinder, J Fluids Eng 120 (2) (1998) 243–252.

[13] G. Karypis, V. Kumar, Multilevel k-way partitioning scheme for irregular graphs., J Parallel Distr Com 48 (1998) 96–129.

[14] A. Kourta, H.C. Boisson, P. Chassaing, H. Ha Minh, Nonlinear interaction and the transition to turbulence in the wake of a circular cylinder, J Fluid Mech 181 (1987) 141–161.

[15] K. Lam, F. Wang, R. So, Three-dimensional nature of vortices in the near wake of a wavy cylinder, J Fluid Struct 19 (2004) 815–833.

[16] O. Lehmkuhl, I. Rodríguez, R. Borrell, J. Chiva, A. Oliva, Unsteady forces on a circular cylinder at critical reynolds numbers, Phys of fluids 26 (2014) 125110.

[17] O. Lehmkuhl, I. Rodríguez, R. Borrell, C.D. Pérez-Segarra, A. Oliva, Low-frequency unsteadiness in the vortex formation of a circular cylinder, Phys Fluids 25 (8) (2013) 085109.

[18] T. Leweke, C.H.K. Williamson, Three-dimensional instabilities in wake transition., Eur J Mech B/Fluids 17 (4) (1998) 571–586.

[19] C. Lewis, M. Gharib, An exploration of the wake three dimensionalities caused by a local discontinuity in cylinder diameter., Phys Fluids 4 (1) (1992) 104–117.

[20] J.-C. Lin, J. Towfighi, D. Rockwell, Instantaneous structure of the near wake of a circular cylinder: on the effect of Reynolds number., J Fluid Struct 9 (1995) 409–418.

[21] X. Ma, G.S. Karamanos, G.E. Karniadakis, Dynamics and low-dimensionality of a turbulent wake, J Fluid Mech 410 (2000) 29–65.

[22] F.M. Najjar, S. Balachandar, Low-frequency unsteadiness in the wake of a normal flat plate., J Fluid Mech 370 (101–147) (1998).

[23] C. Norberg, An experimental study of the flow around cylinders joined with a step in the diameter, 11th Australian fluid mechanics conference, Hobart, Australia, 1992.

[24] C. Norberg, Pressure forces on a circular cylinder in cross flow, IUTAM symposium: bluff body wakes, dynamics and instabilities, Göttingen, Germany, Springer-Verlag, 1993.

[25] C. Norberg, An experimental investigation of the flow around a circular cylinder: influence of aspect ratio., J Fluid Mech 258 (1994) 287–316.

[26] C. Norberg, LDV measurements in the near wake of a circular cylinder, Advances in understanding of bluff body wakes and vortex-induced vibration, Washingtong D.C., USA, 1998.

[27] C. Norberg, Flow around a circular cylinder: aspects of fluctuating lift, J Fluid Struct 15 (2001) 459–469.

[28] A. Papangelou, Vortex shedding from slender cones at low reynolds numbers., J Fluid Mech 242 (1992) 299–321.

[29] H. Persillon, M. Braza, Physical analysis of the transition to turbulence in the wake of a circular cylinder by three-dimensional Navier–Stokes simulation, J Fluid Mech 365 (1998) 23–88.

[30] A. Prasad, C.H.K. Williamson, The instability of the separated shear layer from a bluff body, Phys Fluids 8 (6) (1996) 1347–1349.

[31] A. Prasad, C.H.K. Williamson, Three dimensional effects in turbulent bluff body wakes, J Fluid Mech (343) (1997) 235–265.

[32] S. Rajagopalan, R.A. Antonia, Flow around a circular cylinder–structure of the near wake shear layer, Exp Fluids 38 (2005) 393–402.

[33] I. Rodríguez, R. Borrell, O. Lehmkuhl, C.D. Pérez-Segarra, A. Oliva, Direct numerical simulation of the flow over a sphere at $Re = 3700$, J Fluid Mech 679 (2011) 263–287.

[34] I. Rodríguez, O. Lehmkuhl, R. Borrell, A. Oliva, Direct numerical simulation of a NACA0012 in full stall, Int J Heat Fluid Fl 43 (2013) 194–203.

[35] A. Roshko, On the development of turbulent wakes from vortex streets, NACA rep (1191) (1954).

[36] A. Roshko, Experiments on the flow past a circular cylinder at very high Reynolds number, J Fluid Mech 10 (3) (1961) 345–356.

[37] M. Saad, L. Lee, T. Lee, Shear layers of a circular cylinder with rotary oscillation, Exp Fluids (43) (2007) 569–578.

[38] J.S. Son, T.J. Hanratty, Velocity gradients at the wall for flow around a cylinder at reynolds numbers from 5×10^3 to 10^5, J Fluid Mech 35 (2) (1969) 353–368.

[39] M.C. Thompson, K. Hourigan, J. Sheridan, Three-dimensional instabilities in the wake of a circular cylinder, Exp Thermal and Fluid Science 12 (1996) 190–196.

[40] M.C. Thompson, T. Leweke, C.H.K. Williamson, The physical mechanism of transition in bluff body wakes, J Fluid Struct 15 (2001) 607–616.

[41] F.X. Trias, L. O., A. Oliva, C.D. Pérez-Segarra, R. Verstappen, Symmetry-preserving discretization of Navier–Stokes equations on collocated unstructured grids, J Comput Phys 258 (2014) 246–267.

[42] M.F. Unal, D. Rockwell, The role of the shear layer stability in vortex shedding from cylinders, Phys Fluids 27 (11) (1984).

[43] M.F. Unal, D. Rockwell, Ovortex formation from a cylinder. part 1. The initial instability., J Fluid Mech 90 (1988) 491–512.

[44] R.W.C.P. Verstappen, A.E.P. Veldman, Direct numerical simulation of turbulence at lower costs., J Eng Math 32 (1997) 143–159.

[45] R.W.C.P. Verstappen, A.E.P. Veldman, Symmetry-preserving discretization of turbulent flow, J Comput Phys 187 (1) (2003) 343–368.

[46] C.H.K. Williamson, The natural and forced formation of spot-like 'vortex dislocations' in the transition of a wake, J Fluid Mech 243 (1992) 393–441.

[47] C.H.K. Williamson, Three dimensional wake transition behind a cylinder, J Fluid Mech 328 (1996) 345–407.

[48] C.H.K. Williamson, Vortex dynamics in the cylinder wake, Annu Rev Fluid Mech 28 (1) (1996) 447–539.

[49] H.-Q. Zhang, U. Fey, B.R. Noack, M. König, H. Eckelmann, On the transition of the cylinder wake, Phys Fluids 7 (1995) 779–794.